Int. J. Engng Sci. Vol. 27, No. 10, pp. 1155–1165, 1989
Printed in Great Britain.
0020–7225/89 \$3.00 + 0.00

HISTORIES OF THE STRESS, STRAIN-RATE, TEMPERATURE AND SPIN IN STEADY STATE PENETRATION PROBLEMS

PEI-RONG LIN and R. C. BATRA

Department of Mechanical and Aerospace Engineering and Engineering Mechanics, University of Missouri-Rolla, Rolla, MO 65401-0249, U.S.A.

Abstract—Given the values of the two components of the velocity, temperature, hydrostatic pressure and work-hardening parameter at a large number of discrete points in a bounded 2-D domain, an algorithm has been developed to compute the streamline that passes through a desired point in the domain, and the time histories of the stress, strain-rate, temperature and the spin at a material particle, starting from the instant it occupied the desired point. Results for a few target points situated near the axis of symmetry in the steady state penetration problem involving a viscoplastic target and a rigid cylindrical penetrator are presented. Two nose shapes, namely a hemispherical and blunt, are considered.

INTRODUCTION

One of the choices to be made in the analysis of any mechanics problem is that of the most appropriate constitutive relation for the material of the body. The constitutive relation employed should adequately model the material response over the range of deformations expected to occur in the problem. However, the computed values of the deformation fields generally depend strongly upon the constitutive assumptions made. A way out of this dilemma is to choose a constitutive relation, solve the problem, check if the constitutive assumptions are valid over the range of computed deformations, and, if necessary, resolve the problem with the modified constitutive relation.

In the last few years, many new theories [1–4] of large deformation elasto-plasticity have been proposed. These theories make different kinematic assumptions, thus necessitating the hypothesizing of constitutive relations for variables which may not be simply related with each other. In an attempt to determine which of these theories is the most appropriate for the analysis of penetration problems, we find the histories of the effective stress, second invariant of the strain-rate tensor, the temperature and the spin at a visco-plastic target particle being penetrated by a long rigid cylindrical penetrator. The solution of the steady state problem computed earlier by Batra [5] is presumed to be given.

COMPUTATIONS OF THE STREAMLINES

Let a closed and bounded set $\bar{\Omega} \subset \mathbb{R}^2$ be the domain of interest, and the velocity field be given at a sufficient number of discrete points in $\bar{\Omega}$. That there is a minimum number of points at which the data must be given follows from the observation that the data at two or three discrete points in $\bar{\Omega}$ will certainly not be enough to compute the streamlines passing through an arbitrary given point. The accuracy with which streamlines can be calculated depends strongly upon the number of discrete points at which the data is given. We have not explored the dependence of the error in the streamline upon the number of data points. Thus, the problem to be solved may be stated as follows.

Given the values of the velocity field (V_x, V_y) at a discrete number of points (x^α, y^α), $\alpha = 1, 2, \ldots, M$; find the streamline that passes through an arbitrary point (x_0, y_0).

We note that if the velocity field were given as a continuous function of the position, then the problem would involve integrating the given ordinary differential equations and finding their solution that passes through (x_0, y_0). Since such is not the case here, we assume that the data points can be connected to form disjoint closed polygons $\bar{\Omega}_i$ $(i = 1, 2, \ldots, N)$ with possibly curved sides such that

$$\bar{\Omega} = \bigcup_{i=1}^{N} \bar{\Omega}_{i,}\ \Omega_i \cap \Omega_j = \phi,\ \text{if } i \neq j;\ \lambda(\Omega_i) < \infty, \tag{1}$$

and none of the interior angles of $\bar{\Omega}_i$ is greater than 180°. Here Ω_i equals the interior of the set $\bar{\Omega}_i$, the aspect ratio λ of Ω_i equals the ratio of the diameter of the smallest circle containing Ω_i to the diameter of the largest circle contained in Ω_i. Whereas a theory could possibly be developed for arbitrary polygons Ω_i, we restrict ourselves to the case when Ω_i is a curvilinear triangle obtained by joining six given points such that each of the vertices of the triangle coincides with one of the data points, and each of the sides is a part of a parabolic curve and has a data point as close to its midpoint as possible. The arguments given below do apply to other polygons Ω_i. Hereafter we refer to each of the polygons Ω_i as a finite element.

We assume that $(x_0, y_0) \in \bar{\Omega}$, the point through which the streamline is to be found, is not one of the data points. The first step is to find the $\bar{\Omega}_i$ containing (x_0, y_0) and the components of the velocity at (x_0, y_0). We construct maps

$$T_i : \bar{\Omega}_{\mathrm{M}} \to \bar{\Omega}_i \quad (i = 1, 2, \ldots, N), \tag{2}$$

that are one-to-one and onto, and $\bar{\Omega}_{\mathrm{M}}$ is a right-angled triangle of unit base and unit height. $\bar{\Omega}_{\mathrm{M}}$ is usually referred to as the master triangle or the master element. Referring to Fig. 1, let ϕ_α ($\alpha = 1, 2, \ldots, 6$) be complete quadratic polynomials defined on $\bar{\Omega}_{\mathrm{M}}$ with the property

$$\phi_\alpha(s_\gamma, t_\gamma) = \delta_{\alpha\gamma}, \tag{3}$$

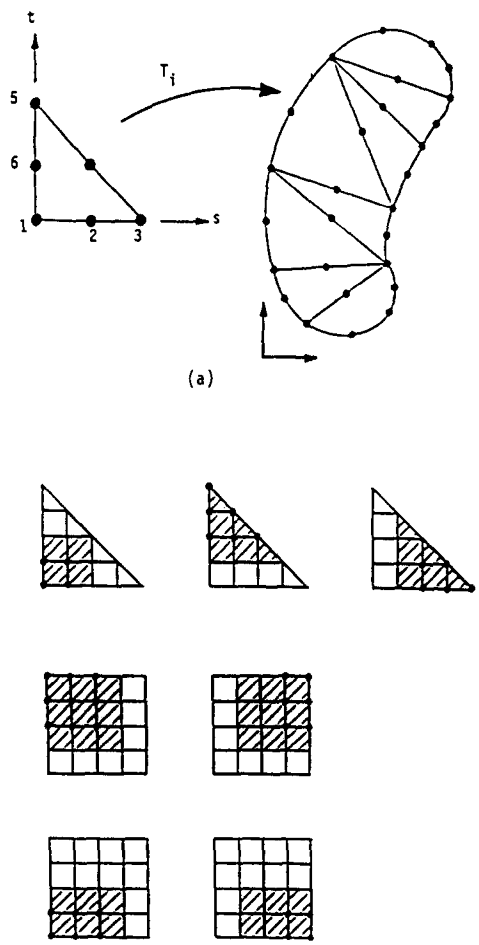

Fig. 1. (a) The master element, discretization of $\bar{\Omega}$ and the node numbering. (b) Possible subregions for further consideration.

where $\delta_{\alpha\gamma}$ is the Kronecker delta. We define the map T_i by

$$x = \sum_{\alpha=1}^{6} x^i_\alpha \phi_\alpha(s, t), \tag{4a}$$

$$y = \sum_{\alpha=1}^{6} y^i_\alpha \phi_\alpha(s, t), \tag{4b}$$

where (x^i_α, y^i_α) are the coordinates of the six data points on $\partial\bar{\Omega}_i$, counted counterclockwise starting with one of the vertices. Under conditions (1) imposed on $\bar{\Omega}_i$, the map T_i defined by eqns (4) is 1–1 and onto [6], and the maps T_i, T_j from $\bar{\Omega}_M$ onto the adjoining elements $\bar{\Omega}_i$ and $\bar{\Omega}_j$ map a side of $\bar{\Omega}_M$ into their common boundary. Thus

$$\bar{\Omega} = \bigcup_{i=1}^{N} T_i(\bar{\Omega}_M). \tag{5}$$

The polynomial functions ϕ_α satisfying (3) are easy to generate and are given in [6]. Unfortunately, it is not easy to solve eqns (4) for s and t in terms of x and y.

We now elaborate upon the procedure used to find $\bar{\Omega}_i$ containing (x_0, y_0) and the local coordinates (s_0, t_0) that correspond to (x_0, y_0) through eqns (4). We subdivide $\bar{\Omega}_M$ by drawing vertical and horizontal lines through $(\frac{1}{4}, 0)$, $(\frac{1}{2}, 0)$, $(\frac{3}{4}, 0)$ and $(0, \frac{1}{4})$ $(0, \frac{1}{2})$ $(0, \frac{3}{4})$, respectively, and use eqns (4) to find the (x, y) coordinates of the 15 points of $\bar{\Omega}_M$ where the horizontal and vertical lines intersect with each other and with the boundaries of $\bar{\Omega}_M$. If (x_0, y_0) is not one of these 15 points in $\bar{\Omega}_i$, we pick out one of the three shaded areas in Fig. 1b such that either (x_0, y_0) is in the image of the shaded area or the distance of (x_0, y_0) from the image of this shaded area is less than the distance of (x_0, y_0) from $\bar{\Omega}_i$. The chosen shaded area $\bar{\Omega}^1_M$ is subdivided as before by drawing horizontal and vertical lines through the quarter points of the two orthogonal sides and the aforementioned selection process is repeated until at the nth iteration one of the following two conditions is satisfied. Either the distance of (x_0, y_0) from $T_i(\bar{\Omega}^n_M)$ is greater than the diameter ρ_n of $\bar{\Omega}^n_M$, in which case we conclude that $\bar{\Omega}_i$ does not contain (x_0, y_0), or ρ_n is smaller than a preassigned small number, in which case we set (x_0, y_0) equal to the average of the x and y coordinates of the vertices of $T_i(\bar{\Omega}^n_M)$. If $(x_0, y_0) \in \bar{\Omega}_i$, then our selection criterion for $\bar{\Omega}^n_M$ ensures that $(x_0, y_0) \in T_i(\bar{\Omega}^n_M)$ for every n. Since $T_i(\bar{\Omega}^{n-1}_M) \subset T_i(\bar{\Omega}^n_M)$ for every n, by Cantor's theorem [7]

$$\lim_{n\to\infty} T_i(\bar{\Omega}^n_M) = (x_0, y_0). \tag{6}$$

Let (s_0, t_0) equal the average of the s and t coordinates of the vertices of $\bar{\Omega}^n_M$. An approximation to the value of the x and y components (V_x, V_y) of the velocity at (x_0, y_0) is

$$V_{x0} = \sum_{\alpha=1}^{6} V^i_{x\alpha} \phi_\alpha(s_0, t_0), \tag{7a}$$

$$V_{y0} = \sum_{\alpha=1}^{6} V^i_{y\alpha} \phi_\alpha(s_0, t_0), \tag{7b}$$

where $V^i_{x\alpha}$ and $V^i_{y\alpha}$ are the given values of the velocity components at the six data points on $\partial\Omega_i$.

In order to compute the streamline through $P(x_0, y_0)$ we must find the point on it adjoining P. With P as center, draw a circle of small radius ε_1 and let the line through P drawn in the direction of the computed velocity $\mathbf{V}_p$ at P intersect the circular arc in Q. If

$$\left| 1 - \frac{|\mathbf{V}_p \cdot \mathbf{V}_Q|}{|\mathbf{V}_p|\,|\mathbf{V}_Q|} \right| \leq \delta, \tag{8}$$

where δ is the prescribed tolerance and $|\mathbf{V}_p|$ is the magnitude of the velocity at P, then Q is the desired neighboring point on the streamline through P (cf. Fig. 2a). If condition (8) is not satisfied at point Q, locate point A on the circular arc distant $\varepsilon_2 \ll \varepsilon_1$ from Q (see Fig. 2b) such that $\vec{QA} \cdot \mathbf{V}_Q > 0$. Draw another circular arc passing through points P and A which is also tangent to $\mathbf{V}_p$ and find the unit tangent vector $\mathbf{U}_t$ to it at the point A. If the computed velocity

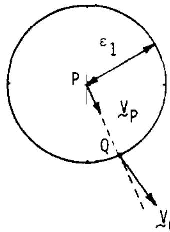

Fig. 2a. The velocity at point Q neighboring point P satisfies condition (8); thus points P and Q lie on a streamline.

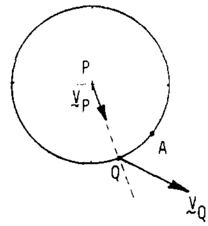

Fig. 2b. Selection of point A if condition (8) is not satisfied.

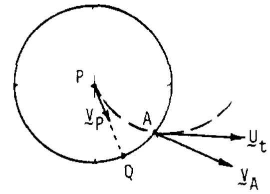

Fig. 2c. The velocity at point A satisfies condition (8); thus points P and A lie on a streamline.

at point A satisfies

$$\left|1 - \frac{|\mathbf{V}_A \cdot \mathbf{U}_t|}{|\mathbf{V}_A|}\right| \leqslant \delta, \tag{9}$$

then A is the desired point adjacent to P. If condition (9) is violated, we find the new position of A along $\vec{QA}$ or $\vec{AQ}$ depending upon the direction of the velocity at A. The procedure is continued until $\mathbf{V}_A \cdot \mathbf{U}_t$ changes sign, and the final position of A is located by using the bisection method.

We note that the interpolation relations (7) can also be used to evaluate the values of other field variables, such as the temperature, from a knowledge of their values at the six data points on $\partial\Omega_i$.

COMPUTATION OF THE HISTORIES OF THE FIELD VARIABLES

Let F stand for one of the quantities such as the second invariant of the strain-rate tensor, temperature or a component of the stress tensor. The problem to be solved is: given the values of the velocity field $(V_x(x^\alpha, y^\alpha),\ V_y(x^\alpha, y^\alpha))$ and $F\ (x^\alpha, y^\alpha)$, $\alpha = 1, 2, \ldots, \mathrm{M}$ at M discrete points (x^α, y^α), find the history of F at a material particle that initially is at an arbitrary point (x_0, y_0).

We solve the problem by first finding the streamline that passes through the point (x_0, y_0) as outlined in the above section. The procedure used to find the streamline also gives $(s, t) \in \bar{\Omega}_{\mathrm{M}}$ which is mapped into the point (x, y) on the streamline by eqn (4). The interpolation relations (7) are then used to find the value of $F(x, y)$.

RESULTS FOR A STEADY STATE PENETRATION PROBLEM

We have developed a computer code based on the algorithm outlined in the preceding sections. The accuracy of the computer code has been ascertained by solving, in a circular domain, the Laplace equation div(grad ϕ) = 0 subjected to essential boundary conditions. The velocity field $\mathbf{v} = \operatorname{grad} \phi$ was computed at discrete points, and used as the input data for the code. The computed streamlines were found to agree very well with the analytical solution.

Below we present streamlines and histories of various field variables for the steady state axisymmetric deformations of a thermoviscoplastic target being deformed by a fast moving rigid cylindrical hemispherical nosed penetrator [5]. In cylindrical coordinates, equations governing the thermomechanical deformations of the target in terms of nondimensional variables are:

$$\operatorname{div} \mathbf{v} = 0,$$

$$\operatorname{div} \boldsymbol{\sigma} = \alpha(\mathbf{v} \cdot \operatorname{grad})\mathbf{v},$$

$$\operatorname{tr}(\boldsymbol{\sigma}\mathbf{D}) + \beta \operatorname{div}(\operatorname{grad} \theta) = (\mathbf{v} \cdot \operatorname{grad})\theta,$$

$$\frac{\operatorname{tr}(\boldsymbol{\sigma}\mathbf{D})}{(1 + \psi/0.017)^n} = (\mathbf{v} \cdot \operatorname{grad})\psi,$$

where

$$\sigma = -p\mathbf{1} + \frac{1}{3I}\left(1 + 10^4\frac{v_0}{r_0}I\right)^{0.025}(1 - 0.000555\theta_0\theta)\left(1 + \frac{\psi}{0.017}\right)^{0.09}\mathbf{D},$$

$$2I^2 = \operatorname{tr}\mathbf{D}^2, \qquad 2\mathbf{D} = \operatorname{grad}\mathbf{v} + (\operatorname{grad}\mathbf{v})^T,$$

$$\sigma = \bar{\sigma}/\sigma_0, \quad p = \bar{p}/\sigma_0, \quad \mathbf{v} = \bar{\mathbf{v}}/v_0, \quad r = \bar{r}/r_0, \quad z = \bar{z}/r_0,$$

$$\theta = \bar{\theta}/\theta_0, \quad \alpha = \bar{\rho}v_0^2/\sigma_0, \quad \beta = \bar{k}/(\bar{\rho}\bar{c}v_0r_0), \quad \theta_0 = \sigma_0/(\bar{\rho}\bar{c}).$$

In these equations the dimensional quantities are indicated by a superimposed bar. Here σ is the Cauchy Stress, ρ is the mass density of a target particle, k is the thermal conductivity, σ_0 is the yield stress in a simple tension or compression test, c is the specific heat, v_0 the speed of the penetrator and r_0 the radius of the penetrator. The values of various parameters used are for a typical steel, viz.

$$c = 473\ \mathrm{J\,kg^{-1}{}^{\circ}C^{-1}}, \quad k = 48\ \mathrm{W\,m^{-1}\,{}^{\circ}C^{-1}}, \quad \rho = 7800\ \mathrm{kg\,m^{-3}}, \quad \sigma_0 = 180\ \mathrm{MPa}.$$

Thus $\theta_0 = 48.9$°C. Results presented below are in terms of nondimensional variables, and for $\alpha = 5$ and $r_0 = 2.54$ mm, $v_0 = 339.7\ \mathrm{m\,s^{-1}}$. Listed below are the multiplying factors in order to obtain dimensional quantities from their nondimensional counterparts.

Quantity	Multiplying Factor
Speed ($\mathrm{m\,s^{-1}}$)	339.7
r or z-coordinate (mm)	2.54
Hydrostatic pressure (MPa)	180
Effective stress (MPa)	180
Strain-rate invariant ($\mathrm{s^{-1}}$)	1.34×10^5
Spin ($\mathrm{s^{-1}}$)	1.34×10^5
Temperature rise (°C)	48.9

Figure 3 shows the three computed streamlines emanating from the points (0.05, 4.27), (0.10, 4.27) and (0.15, 4.27) on the boundary of the finite domain used to analyze the steady state axisymmetric deformations of the thermoviscoplastic target [5]. We note that the target/penetrator interface shown in Fig. 3 is also a streamline. The plotted streamlines show that only within a distance of 0.5 r_0 of the hemispherical part of the penetrator/target interface

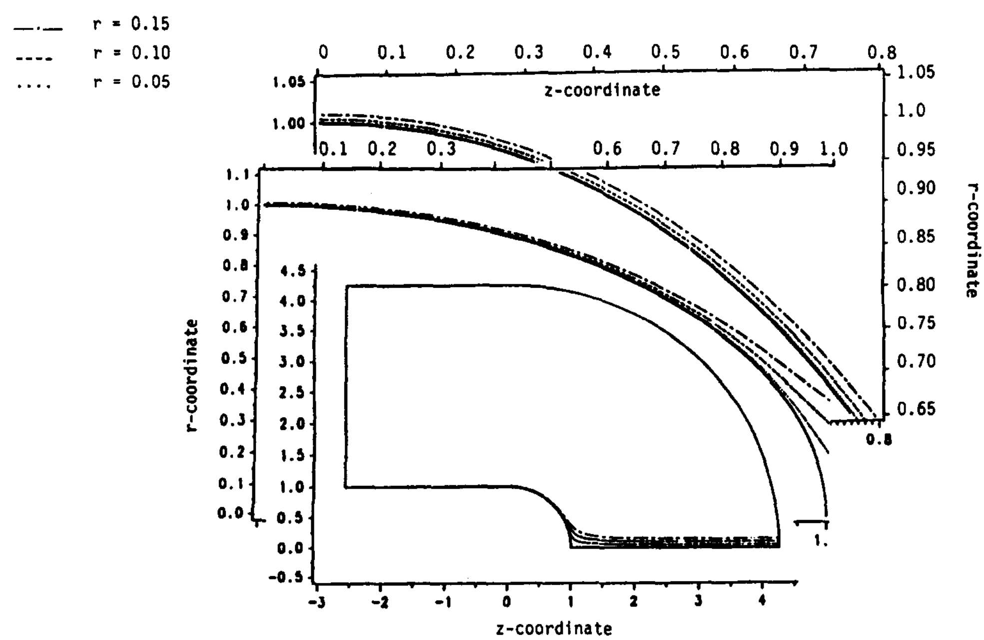

Fig. 3. Streamlines emanating from three points on the boundary of the finite target region being deformed by a rigid cylindrical penetrator with a hemispherical nose.

does the radial component of the velocity of target particles become significant. In order to be able to locate the position of the material particle that was at one of three spatial points initially, we have plotted in Fig. 4 its r- and z-coordinates at various times. Also plotted in this figure is the variation of the speed of the three material particles as seen by an observer situated on the penetrator nose. These plots reveal that the peak value of the absolute speed of target particles decreases as we move away from the axis of symmetry, and this rate of decay of the peak speed slows down as we move away from the axis.

Figures 5 and 6 show the histories of the strain-rate invariant I, the spin, hydrostatic pressure p, work hardening parameter ψ, temperature rise θ and the effective stress s defined as

$$s^2 = \operatorname{tr} \mathbf{s}^2, \qquad \mathbf{s} = \boldsymbol{\sigma} + p\mathbf{1}.$$

The plot of I vs the time t indicates that out of the three material particles considered, the one closest to the axis of symmetry undergoes the severest deformations and the peak value of I suffered by the target particle located farthest from the axis of symmetry is lower as compared to that situated near the axis of symmetry. Since elastic deformations have been neglected in the solution of the penetration problem, the spin plotted in Fig. 5 equals the plastic spin. Its high magnitude as well as that of the hydrostatic pressure signify that one should use an elasto-plasticity theory which accounts appropriately for the plastic spin and the dependence of the yield surface upon the mean stress or the hydrostatic pressure. Referring to Fig. 6, we note that the maximum effective stress s at the three points is equal in magnitude but occurs at slightly different times. The range of temperatures experienced by a material particle is 0 to 550°C, and the maximum temperature of the target particle closest to the axis of symmetry is the highest. Also, the maximum value of the work-hardening parameter ψ is higher for this target particle as compared to that for the other two particles considered.

Batra [5] concluded that the axisymmetric steady state deformations of the viscoplastic target depended strongly upon the penetrator nose shape. Accordingly we investigate here, for a blunt nosed penetrator, the histories of deformation fields for three material particles situated on the target boundary in positions similar to those considered for the hemispherical-nosed penetrator. Figure 7 exhibits streamlines originating from (0.05, 3.48), (0.10, 3.48) and (0.15, 3.48). The three additional drawings in the figure are magnified views of the streamlines around the penetrator nose boundary. As for the hemispherical nosed penetrator, the radial component of the velocity is noticeable only when the particles are within approx. 0.5 r_0 of the

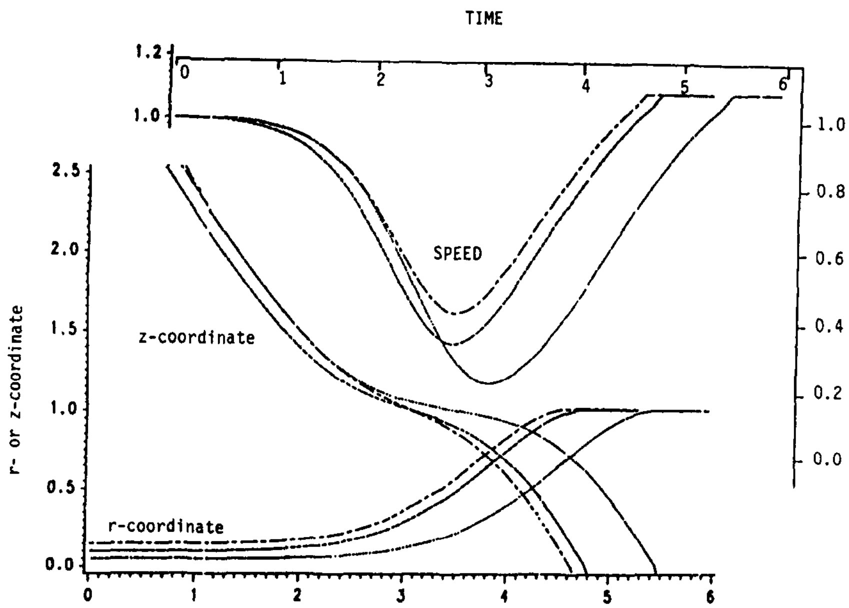

Fig. 4. The variation of speed, and r-, z-coordinates of the three points at different times (hemispherical-nosed penetrator).

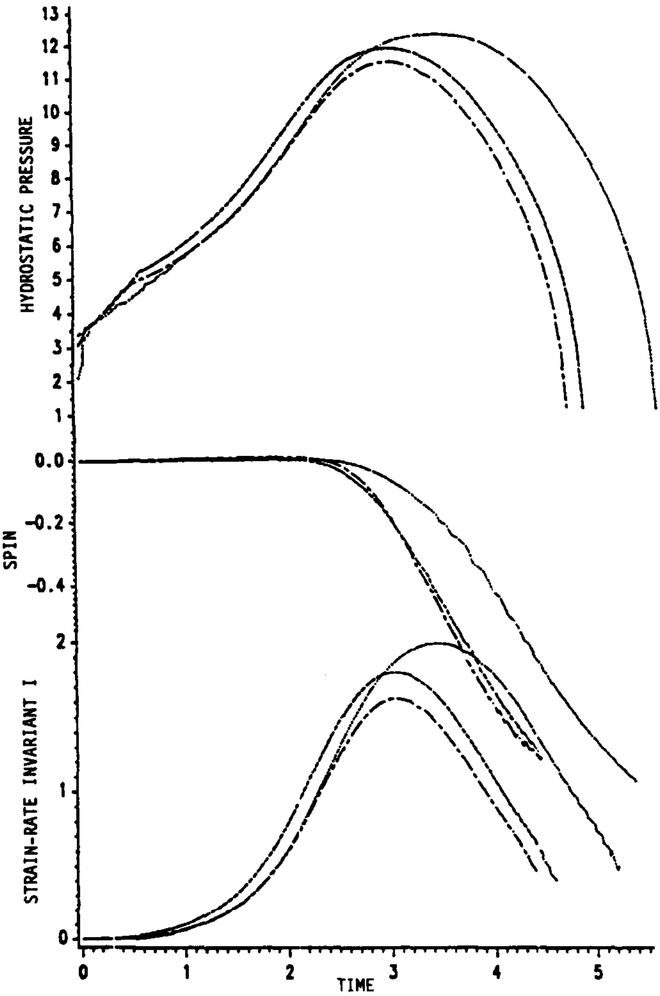

Fig. 5. Histories of the hydrostatic pressure, the spin and the strain-rate invariant I (hemispherical-nosed penetrator).

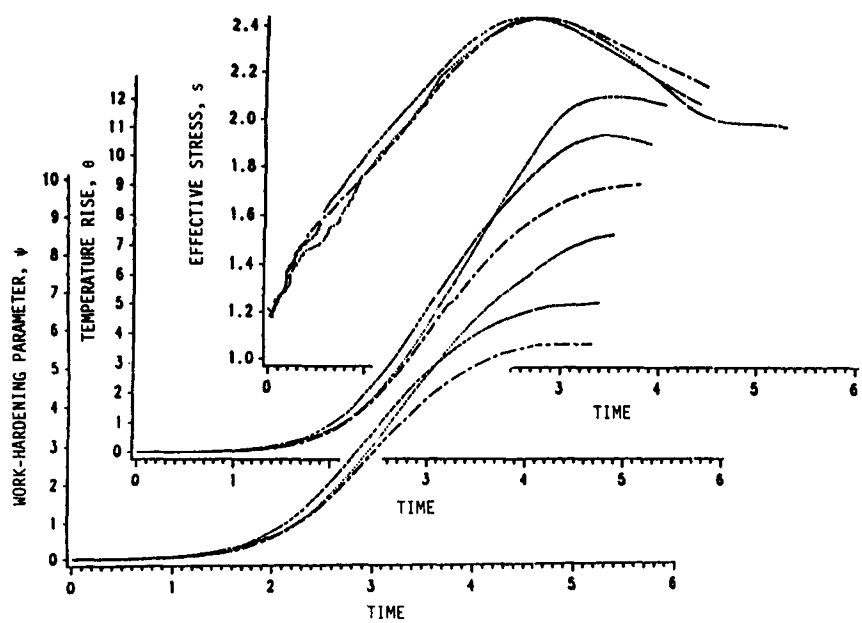

Fig. 6. Histories of the work-hardening parameter, temperature rise and the effective stress (hemispherical-nosed penetrator).

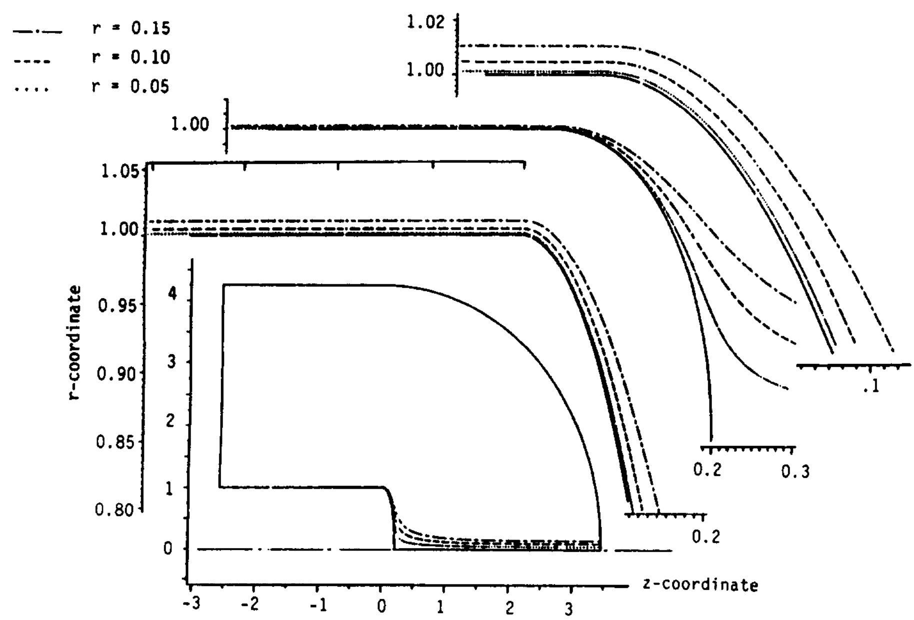

Fig. 7. Streamlines originating from three points on the boundary of the finite target region being deformed by a rigid cylindrical penetrator with a blunt nose.

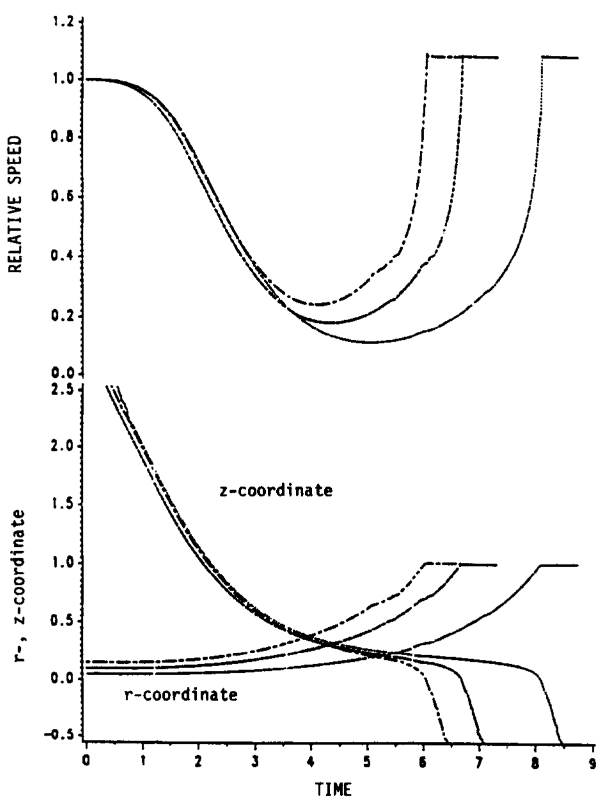

Fig. 8. The variation of speed, and r-, z- coordinates of the three points at different times (blunt nosed penetrator).

target/penetrator interface. Figure 8 gives the variation of the speed of the three particles as well as their (r, z) coordinates at different times; the time being clocked from the instant they occupy the indicated positions on the target boundary. The histories of the strain-rate invariant I and the spin plotted in Fig. 9 along with the data plotted in Fig. 8 indicate vividly that the material particles undergo severe deformations when they are near the boundary of the penetrator nose. Both their speeds and velocity gradients are quite high in this region. The strain-rate invariant and the spin drop sharply as the material particles move outwards and away from the boundary of the penetrator nose.

Figure 10 shows the histories of the temperature rise θ and the work-hardening parameter ψ at the three material particles. Like the hemispherical-nosed penetrator, of the three material particles studied, the one closest to the axis of symmetry experiences the highest value of θ and ψ. These peak values occur after the material particle has traveled away from the boundary of the penetrator nose where I is quite high. Even though plastic working is highest near the penetrator nose boundary, because of the advection of heat, the maximum temperature occurs when the material particle is a little bit away towards the rear of the penetrator. We have plotted the histories of the hydrostatic pressure and the effective stress in Fig. 11. The peak hydrostatic pressure occurs when the material particle is near the penetrator nose boundary and towards the axis of the penetrator. The pressure drops suddenly as the particle moves away from the penetrator nose boundary. Recalling that the nose shape is blunt or virtually flat, the singular behavior of the normal stress of which the hydrostatic pressure is a predominant part is to be expected. The importance of considering the thermal softening in the constitutive relation is borne out by the histories of the effective stress s. A glance at Figs 9–11 reveals that while I, θ and ψ at a material particle are increasing, s is decreasing, implying thereby that the softening caused by the heating has overcome the combined effects of work and strain-rate hardening. It is very likely that a material instability in the form of an adiabatic shear band [8, 9] will initiate somewhere near the boundary of the penetrator nose. That there is more likelihood of a shear band being formed for a flat nosed penetrator as compared to that for hemispherical-and ogival-nosed penetrators was experimentally observed by Wingrove [10].

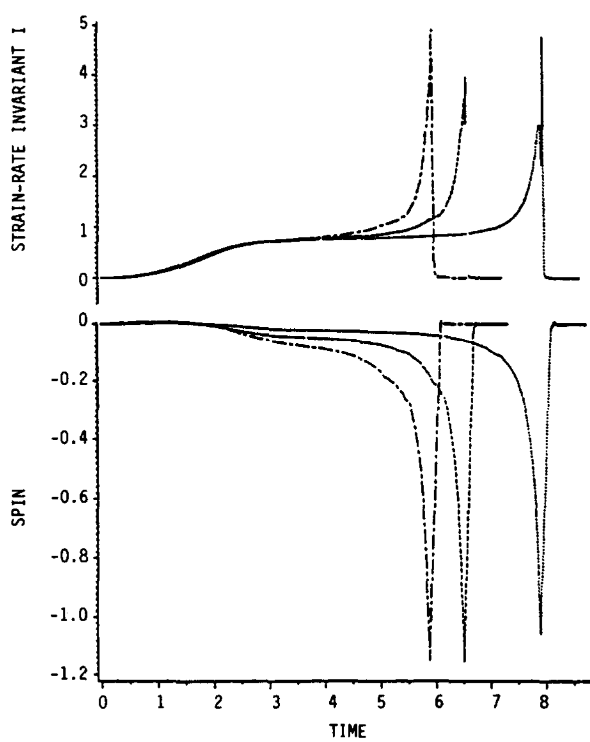

Fig. 9. Histories of the spin and the strain-rate invariant at the three target particles (blunt-nosed penetrator).

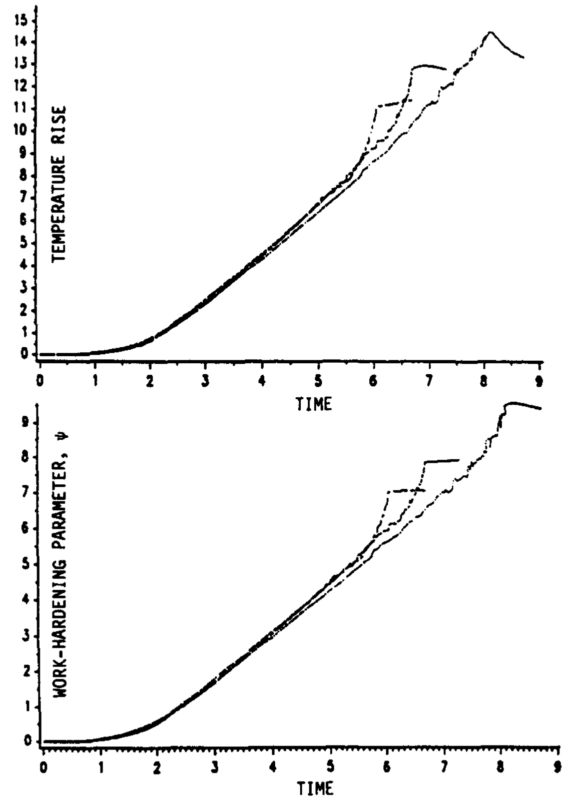

Fig. 10. Histories of the temperature and the work-hardening parameter at the three target particles (blunt-nosed penetrator).

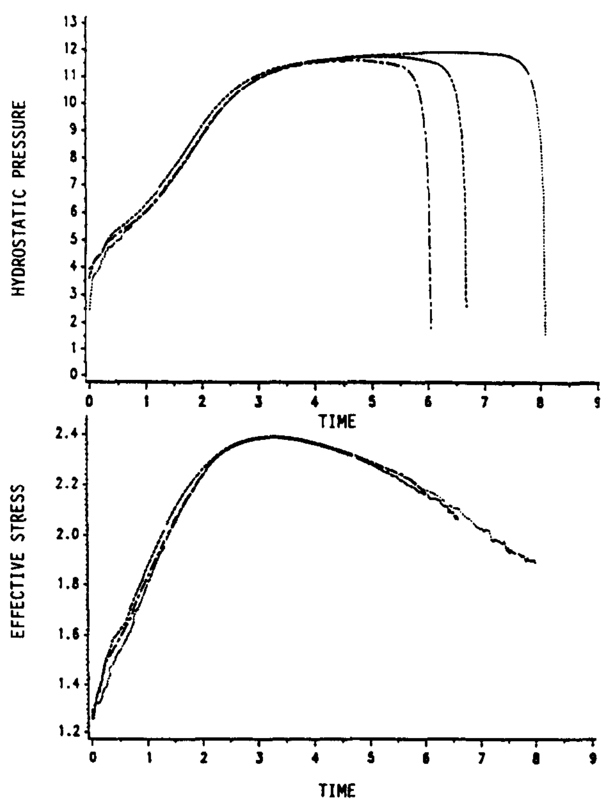

Fig. 11. Histories of the hydrostatic pressure and the effective stress at the three target particles (blunt-nosed penetrator).

CONCLUSIONS

Both for the hemispherical-nosed and the blunt-nosed rigid penetrators, the target particles undergo plastic spin comparable to the strain-rate invariant I, and the peak hydrostatic pressure equals nearly 12 times the yield stress of the target material. Thus, plasticity theories which properly account for the plastic spin and the effect of high hydrostatic pressure should be used to assess the importance of these factors on the solution of the penetration problem. It seems that there is a greater likelihood of the formation of an adiabatic shear band near the penetrator/target interface for the blunt-nosed penetrator as compared to that for the one with a hemispherical nose.

Acknowledgements—R. C. Batra is indebted to Drs T. W. Wright and John Walter Jr, of the U.S. Army Ballistic Research Laboratory for suggesting the problem. Pei-Rong Lin is grateful to Professor Troy Hicks for useful discussions regarding Cantor's theorem. Some of these computations were performed on the National Science Foundation Supercomputer Center at the University of Illinois-Urbana. This work was partially supoorted by the U.S. Army Research Office Contract DAAG 29-85-K-0238 to the University of Missouri-Rolla, and a U.S. Army Ballistic Research Laboratory STAS Contract to R. C. Batra.

REFERENCES

[1] E. H. LEE, *J. Appl. Mech.* **36**, 1 (1969).
[2] L. ANAND, *J. Appl. Mech.* **47**, 439 (1980).
[3] S. NEMAT-NASSER, *Proc. Symp. Plasticity Today* (Edited by A. SAWCZUK). Elsevier Applied Science, London (1983).
[4] Y. F. DAFALIAS, *Proc. Current Theories of Plasticity and Their Applications*, University of Oklahoma-Norman (1984).
[5] R. C. BATRA, *Comput. Mech.* **3**, 1 (1988).
[6] E. BECKER, G. CAREY and J. T. ODEN, *Finite Elements—An Introduction*, Vol. 1. Prentice-Hall, Englewood Cliffs, New Jersey (1983).
[7] J. C. BURKILL and H. BURKILL, *A Second Course in Mathematical Analysis*, p. 55. Cambridge University Press (1970).
[8] R. C. BATRA, *Int. J. Plasticity* **3**, 77 (1987).
[9] R. C. BATRA and CHANG-HO KIM, *Int. J. Plasticity* In press.
[10] A. L. WINGROVE, *Metall. Trans.* **4**, 1829 (1973).

(*Received* 4 *January* 1989)